
LHU-NET: A LIGHT HYBRID U-NET FOR COST-EFFICIENT, HIGH-PERFORMANCE VOLUMETRIC MEDICAL IMAGE SEGMENTATION

Yousef Sadegheih^{†1}, Afshin Bozorgpour^{†1}, Pratibha Kumari¹, Reza Azad², and Dorit Merhof^{*1,3}

¹Faculty of Informatics and Data Science, University of Regensburg, Regensburg, 93053, Germany

²Faculty of Electrical Engineering and Information Technology, RWTH Aachen University, 52062 Aachen, Germany

³Fraunhofer Institute for Digital Medicine MEVIS, Bremen 28359, Germany

ABSTRACT

The rise of Transformer architectures has revolutionized medical image segmentation, leading to hybrid models that combine Convolutional Neural Networks (CNNs) and Transformers for enhanced accuracy. However, these models often suffer from increased complexity and overlook the interplay between spatial and channel features, which is vital for segmentation precision. We introduce LHU-Net, a streamlined Hybrid U-Net for volumetric medical image segmentation, designed to first analyze spatial and then channel features for effective feature extraction. Tested on five benchmark datasets (Synapse, LA, Pancreas, ACDC, BRaTS 2018), LHU-Net demonstrated superior efficiency and accuracy, notably achieving a 92.66 Dice score on ACDC with 85% fewer parameters and a quarter of the computational demand compared to leading models. This performance, achieved without pre-training, extra data, or model ensembles, sets new benchmarks for computational efficiency and accuracy in segmentation, using under 11 million parameters. This achievement highlights that balancing computational efficiency with high accuracy in medical image segmentation is feasible. Our implementation of LHU-Net is freely accessible to the research community on [GitHub](#).

Keywords Volumetric Medical Image Segmentation, Deep Learning, Computational Efficiency, High-Performance Segmentation, Light Hybrid Architecture

1 Introduction

Medical imaging technologies such as MRI, CT, or planar X-ray imaging, have substantially transformed diagnostics by providing non-invasive visualizations of internal anatomical structures. Segmentation of medical imaging data is commonly performed to support diagnostics, intervention planning, or disease progression assessment. However, manual segmentation by radiologists is not only time-consuming, but is also highly subjective and prone to inconsistencies. Accordingly, there is a growing need for automated segmentation approaches.

Recently, deep learning approaches (and Convolutional Neural Networks (CNNs) in particular) have shown great potential for medical image segmentation. Prominent CNN-based segmentation networks include Fully Convolutional Networks (FCNs) (Long et al. 2015), U-Net (Ronneberger et al. 2015), DeepLab (Liang-Chieh et al. 2015), ResNet (He et al. 2016), and V-Net (Milletari et al. 2016). Each of these network designs has made significant progress by consistently outperforming earlier state-of-the-art networks (Azad et al. 2022, Bozorgpour et al. 2023).

Although CNNs can detect local patterns, they are fundamentally unable to comprehend the wider context or global connections present in an image. This constraint becomes especially apparent while performing intricate image analysis tasks that require a comprehensive understanding of the entire scene or image. The Vision Transformer (ViT) (Dosovitskiy et al. 2020) design has been central to recent developments aimed at overcoming this constraint.

*Corresponding author: Dorit Merhof, *e-mail*: dorit.merhof@ur.de

† *Indicates equal contribution*

The attention mechanism is the spine of ViT’s architecture which allows the aggregation of data over the whole input sequence. Overcoming the limited receptive field limitations commonly seen in CNNs, this strategy enables the network to absorb long-range contextual information (Shamshad et al. 2023). Nevertheless, here a major drawback is set by the underrepresentation of local information hence compromising the performance (Azad et al. 2023a). This is more noticeable when it comes to detecting local textures with a fine grain, which is an essential component of many diagnostic and prognostic activities (Azad et al. 2023b). This restriction stems from the fact that ViTs use a novel approach to image processing. To comprehend the inter-dependencies among the image’s patches, ViT models use self-attention mechanisms to break the image into smaller pieces. Although ViTs have made advancements in capturing overall contextual information, CNNs may have an advantage in extracting specific features within a local area because of the differences in their fundamental methods for image processing (Geirhos et al. 2018).

Consequently, there has been a paradigm shift towards hybrid models that amalgamate the strengths of both CNNs and vision transformer models (Geirhos et al. 2018). A notable strategy involves the fusion of CNN and transformer model features, leveraging the local feature extraction capabilities of CNNs and the global contextual understanding of transformers. This synergy aims to overcome the individual limitations of each architecture. For instance, TransUNet (Chen et al. 2021), an innovative architecture, merges transformer layers within the CNN bottleneck, enabling the simultaneous modeling of both local and global dependencies. Another exemplary model, HiFormer (Heidari et al. 2023), introduces the integration of a Swin transformer module with a CNN-based encoder. This architecture generates dual multi-scale feature representations, which are then coalesced through a Double-Level Fusion module, enhancing the overall segmentation accuracy. Further, architectures like UNETR (Hatamizadeh et al. 2022) and CoTr (Xie et al. 2021) have been instrumental in advancing 3D medical image segmentation. UNETR utilizes a transformer-based encoder in tandem with a CNN decoder, optimizing the segmentation process. CoTr, on the other hand, innovatively bridges a CNN encoder and decoder with a transformer, specifically targeting an enhanced performance in low-resolution stages of segmentation. Furthermore, TransBTS (Wang et al. 2021) represents another stride in this direction, employing a similar hybrid approach to optimize segmentation results. Additionally, architectures such as Swin-UNet (Cao et al. 2022) offer unique advantages. The Swin transformer’s shifted window-based self-attention mechanism within a U-Net-like architecture facilitates the efficient handling of large-scale medical images while capturing intricate details and broad structural contexts, making it highly effective for complex segmentation tasks.

CNNs are distinguished by their hierarchical architecture, adept at discerning spatial hierarchies in imagery via convolutional filters, benefiting from their inherent translation invariance and localized connectivity. This design tends to yield models characterized by a reduced parameter count due to the sharing of weights across spatial domains and the confinement of convolution operations to localized areas. As a result, CNNs generally demand less computational power, particularly in applications where spatial coherence is pivotal. Conversely, ViTs employ self-attention mechanisms, which, although offering comprehensive analysis capabilities across an image, cause a quadratic surge in computational costs relative to the input size. This attribute renders ViTs more demanding in terms of computationally and parameter volume. Hybrid models seek to amalgamate CNNs’ local processing efficiencies with ViTs’ expansive global receptive fields. Yet, this ambition often culminates in a marked escalation of parameters and computational expenditure. Certain hybrid models indiscriminately increase model complexity, adding layers or expanding attention mechanisms across the network in the hope of boosting performance. This brute-force scaling-up strategy often results in diminishing returns on performance gains relative to the higher computational overhead (Zhou et al. 2023, Yang et al. 2024, Chen et al. 2023, Shaker et al. 2024). The insufficiency of current hybrid models, particularly in the context of volumetric medical image segmentation, may well stem from their sub-optimal self-attention configurations. Moreover, these models typically fail to explicitly leverage the interplay between spatial and channel features, an oversight that could otherwise improve segmentation accuracy. A refined strategy adapts attention mechanisms to suit various model stages. Initially, where the acquisition of spatial information is crucial, specialized attention blocks tailored for spatial focus can effectively manage local features. As the model delves deeper, the emphasis shifts towards assimilating broader contextual data, necessitating attention frameworks that prioritize channel dynamics. Such sequential customization facilitates a harmonious balance between model intricacy and efficacy. Aligning architectural design with the specific demands of information processing at each stage enables enhanced performance, circumventing the disproportionate parameter and computational load increase seen in more homogenized hybrid models. In essence, the evolution of hybrid models offers a promising avenue to exploit the unique strengths of both CNNs and ViTs. Nevertheless, simply amplifying model complexity fails to serve as a panacea. Instead, a meticulously crafted network featuring bespoke attention mechanisms attuned to the distinct requirements of varying processing phases emerges as a more adept and resource-efficient methodology for capitalizing on the synergistic potential of CNNs and ViTs in visual data analysis.

In this context, we introduce LHU-Net (Light Hybrid U-Net), a model that achieves a balance between complexity and performance. LHU-Net shows that it is possible to reach an optimal balance, setting a new standard in the design of hybrid models for complex image segmentation tasks.

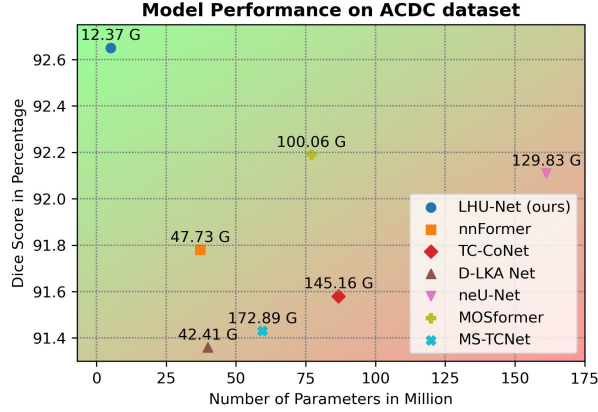


Figure 1: Comparison of model performance on the ACDC dataset, showing the Dice Score (in percentage) against the number of parameters (in millions) for different models. The numbers above each marker represent the computational cost in terms of FLOPS (in billions). LHU-Net (ours) achieves the highest Dice Score with the fewest parameters and lowest FLOPS, highlighting its efficiency and accuracy.

Contributions

This work introduces key advancements in medical image segmentation, enhancing both efficiency and accuracy. The main contributions are:

❶ **Efficient Hybrid Attention Selection for Better Contextual Understanding:** Our approach uses two specialized attention mechanisms within Vision Transformers (ViTs) to improve the understanding of both local and global contexts. By integrating Large Kernel Attention with an extra deformable layer alongside spatial and channel attention, our model can effectively handle long-range dependencies and maintain high-frequency details. Initially, the model uses spatial attention to capture local features in the early layers. As the model progresses to deeper layers, it shifts to channel attention to highlight important features. This combined strategy helps LHU-Net effectively use the strengths of both spatial and channel attention, ensuring a comprehensive feature extraction process suited for the demands of medical image segmentation.

❷ **Setting New Efficiency Benchmarks in Medical Segmentation:** LHU-Net achieves high-performance segmentation with reduced computational resources. In the Automated Cardiac Diagnosis Challenge, it reduces parameters by about **85%** and **quarters** the FLOPS (see Figure 1). Across all benchmarked datasets, the model maintains a parameter count of less than 11 million, demonstrating that a well-designed model can achieve high performance without high computational demands.

❸ **Versatile Superiority Across Diverse Imaging Modalities and Segmentation Challenges:** LHU-Net performs well across various datasets, including CT scans, MR images, and multimodal datasets like BraTS. It handles tasks ranging from single-label to multi-label segmentation, demonstrating its robustness and adaptability as a universal solution for medical image segmentation.

In summary, LHU-Net advances medical image segmentation by offering a scalable, efficient model that addresses computational efficiency and adaptability, making deep learning solutions more accessible for clinical use.

2 Methodology

Our approach, named LHU-Net, is designed to efficiently extract enriched features across various network levels while optimizing parameter efficiency. By combining convolutional-based blocks with hybrid attention mechanisms, LHU-Net captures both local and broader contextual information. Figure 2 illustrates the architecture of LHU-Net, showcasing its hierarchical U-Net encoder-decoder structure. The encoder stages process 3D input patches into different levels of detail, from local to global, and pass important information through skip connections to the decoder stages, which then create the final segmentation masks. Table 1 shows the notations used throughout this section.

Network Architecture: LHU-Net comprises three distinct stages respecting the spatial dimensions of the feature map. The first stage includes the “Init Block,” and “Out Block,” located at the beginning and end of the network. This stage maintains the size of the input and output feature maps, ensuring that the input shape is preserved throughout the network for accurate data transformation in the encoder and desired output in the decoder. At the intermediate

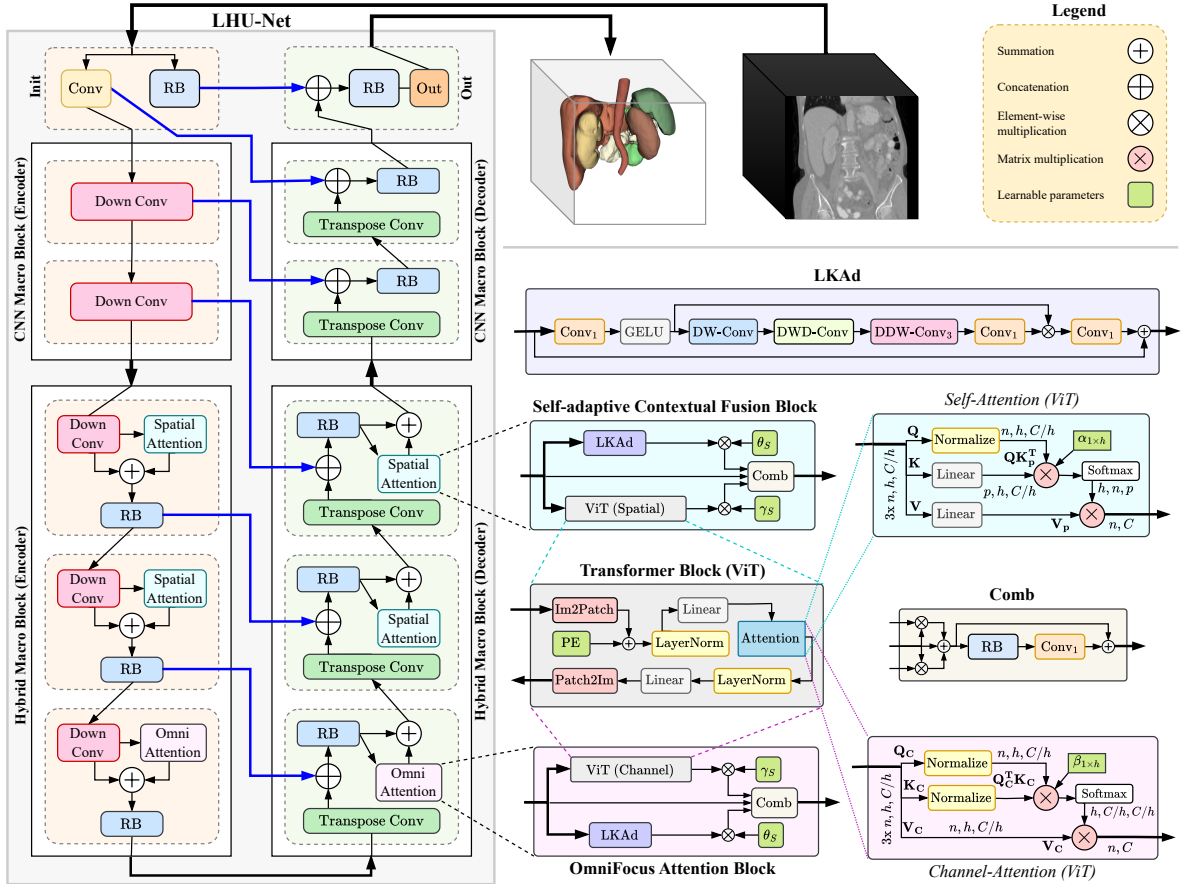


Figure 2: The proposed LHU-Net architecture. On the left, an abstract representation of the proposed network is depicted. At the top levels, the ‘Init’ and ‘Out’ blocks manage input and output respectively, while ‘CNN Macro Blocks’ facilitate information flow between these top-level blocks and the ‘Hybrid Macro Blocks’ at the network’s core. Thorough explanations of the utilized attention blocks and their sub-components, along with other relevant details, are provided on the right side of the network, offering a comprehensive understanding of the architecture’s design. Note that ‘PE’ and ‘RB’ stand for Positional Embedding and ResBlock, respectively.

stage, convolutional blocks (termed “CNN Blocks”) reduce the size of the feature maps while improving local features, effectively capturing high-frequency details. The final stage, named “Hybrid Blocks,” uses three types of attention mechanisms. These include convolutional large kernel attention (Guo et al. 2023) with one additional deformable layer (Azad et al. 2024) alongside spatial and channel-wise ViT attention blocks, further refines features, accounting for global representations and long-range dependencies. Throughout the encoder stages, skip connections maintain connectivity with corresponding decoder blocks, ensuring seamless information flow. Detailed explanations of each stage are provided in the following subsections.

2.1 Init and Out Blocks

To optimize the performance of subsequent convolutional blocks in the deeper levels of the network and enhance the overall quality of the final output, special emphasis is placed on the boundary regions by employing the *Init* and *Out* stages. These stages ensure that all processing is conducted within the same spatial space as the input image, preserving its spatial dimensions while boosting the model’s effectiveness. The *Init* block begins with a point-wise convolutional operation (PW-Conv) applied to the input data, adjusting the channel dimensions to match those of the subsequent level.

$$F_1 = \text{BN}(\text{PReLU}(\text{PW-Conv}(I))) \quad (1)$$

Table 1: Key notations used throughout Section 2, color-coded for clarity: green signifies convolutional layers and blocks, magenta represents transformers and attention mechanisms, orange denotes activation functions, and blue highlights variables and parameters.

Acronym	Meaning
BN	Batch normalization layer
<i>PW-Conv</i>	Point-wise convolution block
<i>DW-Conv</i>	Depth-wise convolution block
<i>DWD-Conv</i>	Depth-wise dilated convolution
<i>DDW-Conv</i>	Deformable depth-wise convolution
<i>ResBlock</i>	Residual Block
<i>LKAd</i>	Large kernel attention with one additional deformable layer
ViT	Vision transformer
<i>A</i>	Self-attention matrix
<i>CA</i>	Channel attention module
<i>SA</i>	Self-attention module
<i>PE</i>	Positional embedding
<i>GELU</i>	Gaussian error linear unit
<i>PReLU</i>	Parametric rectified linear unit
<i>n</i>	Number of tokens (<i>HW</i> <i>D</i>)
<i>h</i>	The number of heads in the ViT attention block
<i>x</i>	Input variable
<i>d</i>	Hidden state dimension
<i>Q</i>	The query embedding inputs
<i>K</i>	The key embedding inputs
<i>V</i>	The value embedding inputs
<i>S</i>	The skip connection
<i>F</i>	The feature map

Here, F_l is of the same spatial size as I (the input image). It represents the feature map produced directly from the input image, serving as the input for subsequent levels and acting as the skip connection for the last step of the CNN Decoder Block simultaneously.

Moreover, the model uses a ResBlock directly on the input data to extract high-frequency details that capture important local features. This approach helps in identifying key details needed for accurate boundary estimation in the final segmentation output. These details are then passed to the *Out* block, as shown in the equation below, which aids in guiding the final mask (X_{Out}).

$$X_{Out} = \text{PW-Conv}(\text{ResBlock}(\text{ResBlock}(I) + X_{CD})) \quad (2)$$

Here, X_{CD} represents the output of the CNN Decoder Block.

2.2 CNN Blocks

A key part of our model is the pure CNN blocks, which are known for effectively capturing strong local contextual features at high and mid-frequency levels. Unlike methods that use only ViT, our approach includes ResBlocks at two levels to reduce spatial dimensions without losing feature details, preparing the input for the next hybrid stage. This approach is based on two reasons: Firstly, the initial large spatial dimensions are computationally expensive and do not efficiently use spatial ViT blocks, nor do they achieve the detailed channel representation needed for effective channel-wise ViT attention blocks. Secondly, by not downsampling in the *Init* block, we focus on using parameters efficiently and preserving local features, leaving the capture of more global features to the next level.

At each level of the encoder (l), the *Down Conv* block encodes the input feature F_l into the output feature F_{l+1} as defined:

$$\begin{aligned} \hat{F} &= \text{BN}(\text{DW-Conv}(\text{LeakyReLU}(\text{BN}(\text{DW-Conv}_{\text{Down}}(F_l)))))) \\ R &= \text{BN}(\text{PW-Conv}(F_l)) \\ F_{l+1} &= \text{LeakyReLU}(\hat{F} + R) \end{aligned} \quad (3)$$

where, $\text{DW-Conv}_{\text{Down}}$ denotes the convolution operation responsible for downsampling the spatial dimensions of F_l . \hat{F} represents the processed feature map obtained by applying normalization, convolution, and activation functions to

the downsampled feature map F_l . R captures the original input feature F_l after a normalization and convolutional operation. Finally, F_{l+1} is computed by adding the processed feature map \hat{F} to the original feature map R , followed by an activation function. Also, Equation (3) can be considered A ResBlock operations when $R = F_l$. This process facilitates the flow of information while efficiently managing spatial dimensions across different levels of the encoder.

2.3 Hybrid Blocks (Hybrid Attention)

Carefully integrating the LKAd module within the network, especially in the intermediate to deep layers, significantly enhances the network’s ability to perform semantic segmentation. This is crucial for accurately identifying the boundaries and objects within an image by balancing local details with global context.

In this final stage of the network, which includes intermediate and deep layers, we focus on using hybrid attention techniques. After establishing a strong base for capturing local features in the earlier stage, we now expand to include various attention mechanisms.

We incorporate larger kernel sizes to capture a wider range of spatial representations and use deformable methods to maintain focus on the desired receptive fields. At the same time, spatial ViT attention is used in the initial layers of this stage, and channel ViT attention is employed in the final layers. This combination helps in aggregating detailed and high-level descriptions within the channels, facilitating the extraction and integration of the most important features and details.

This strategic arrangement enhances efficiency by carefully selecting appropriate combinations across different layers, avoiding the need for repeated use of fixed blocks (Shaker et al. 2024, Rahman et al. 2024, Liu et al. 2024) or multiple repetitions (Azad et al. 2024, Wang et al. 2023a, Hong et al. 2023, Li et al. 2023) across levels. This method allows us to capture nuanced and meaningful features while maintaining complexity and minimizing the number of parameters, facilitating effective learning. By interacting with diverse representative feature maps at different levels, we avoid the limitations of a single fixed module design, which often fails to be responsive and efficient without incorporating various considerations, leading to suboptimal performance. Some approaches attempt to improve generality and results by repeating modules, but this increases the number of parameters and reduces efficiency. Instead, we have designed level-specific modules to be used within the network without repetition or redundancy. This ensures that each level’s unique features are effectively captured, maintaining complexity and minimizing parameters, thereby facilitating effective learning and achieving optimal results.

2.3.1 Self-Adaptive Contextual Fusion Module

Adding the spatial attention block within the top hybrid blocks, both residually in the encoder stage and collectively in the decoder stage, along with the convolutional information flow, strengthens the model’s ability to handle global structures. This setup captures global contextual information effectively by merging spatial attention maps, computed in parallel using the outputs of LKAd and self-attention mechanisms. This block helps prevent information loss, especially in the deeper layers of the encoder, and smoothly transfers features to the CNN Blocks in the decoder.

In the spatial attention block, we use the LKAd block together with spatial self-attention. This combination allows the model to handle long-range dependencies, extract comprehensive global contextual representations, and reduce texture bias, while effectively extracting features and maintaining high-frequency representation. LKAd considers large regions within the input image in a flexible and adaptive way, allowing for a broader receptive field by using a deformable grid after two convolution layers of LKAd, unlike standard attention mechanisms that are limited to fixed-size regions. This adaptability enables the block to efficiently capture local and global contextual information.

As depicted in Figure 2, the final output of the Self-adaptive Contextual Fusion block is computed as:

$$F_S = \text{Comb}(F, \delta_s \text{LKAd}(F) + \gamma_s \text{SA}(F)) \quad (4)$$

Where $F \in \mathbb{R}^{C \times H \times W \times D}$ represents the input feature maps, and F_S denotes the output of this block with the same dimensions. δ_s and γ_s represent learnable parameters per channel that control the combination weights of the two different attention mechanisms.

LKAd: This module handles attention computation as outlined in (Azad et al. 2024), using the following steps::

$$\begin{aligned} \hat{x} &= \text{GELU}(\text{PW-Conv}(x)) \\ x_{\text{LA}} &= \text{DWD-Conv}(\text{DW-Conv}(\hat{x})) \\ x_{\text{LKAd}} &= \text{PW-Conv}(\text{DDW-Conv}_3(x_{\text{LA}})) \\ x_{\text{Ad}} &= \text{PW-Conv}(x_{\text{LKAd}} \otimes \hat{x}) + x, \end{aligned} \quad (5)$$

where the input tensor $x \in \mathbb{R}^{C \times H \times W \times D}$ goes through several transformations to enhance its representational capacity and contextual understanding. First, the input is subject to a pointwise convolution operation, denoted as Conv_1 , followed by an activation function, Gaussian Error Linear Units ($GELU$), to induce nonlinearity and dimensionality reduction. The transformed tensor \hat{x} is then processed through a sequence of depth-wise convolutions ($DW\text{-Conv}$) and depth-wise dilated convolutions ($DWD\text{-Conv}$) to extract multi-scale features while preserving spatial information. The resulting tensor x_{LA} encapsulates locally attentive representations. Notably, the distinctive aspect of the LKAd module lies in its integration of deformable depth-wise convolutions ($DDW\text{-Conv}$), denoted as $DDW\text{-Conv}_3$, which introduces deformable grids to enable adaptive sampling of feature maps. This enhances the model’s ability to capture fine details and long-range dependencies. Finally, the element-wise operations \otimes (multiplication) and $+$ (summation) are used to combine the refined feature map x_{LKAd} with the original input \hat{x} through a pointwise convolution. This fusion of global contextual information with local features results in the tensor x_{Ad} , which enriches the representation of the input tensor x .

Self-Attention: The self-attention module, denoted as SA , computes the final result $SA(x)$ using a normalized tensor x of shape n, C , where $n = H \times W \times D$. This involves generating Q , K , and V projections through three linear layers, each with dimensions $n, h, C/h$, where h is the number of heads. The projections are computed as $Q = W^Q X$, $K = W^K X$, and $V = W^V X$, with W^Q , W^K , and W^V being the projection weights for Q , K , and V , respectively. To manage complexity and efficiently learn spatial information, a technique proposed in (Shaker et al. 2024) is employed, which involves two additional projections for K and V . This results in $K_p = W_K^p \times K$ and $V_p = W_V^p \times V$, transforming the n spatial tokens from K and V into p learnable complex spatial separations in K_p and V_p , changing the dimensions from $n, h, C/h$ to $p, h, C/h$, where $p \ll n$. Next, the normalized Q is multiplied by the transpose of K_p and the resulting values are adjusted using the learnable parameter α . After applying a softmax function (σ), the similarity between each feature and the remaining spatial features is obtained. Finally, these computed similarities are multiplied by the projected V layer to produce the final spatial attention with dimensions $n \times C$. This spatial attention mechanism is described by the equation:

$$x_{SA} = \sigma \left(\frac{Q K_p^T}{\sqrt{d}} \right) \cdot V_p \quad (6)$$

Here, Q , K_p , and V_p stand for queries, projected keys, and projected spatial value layers, respectively, each of size d . Next, we pass x_{SA} through a linear normalization followed by a linear layer to enhance the performance as the result of SA module. Finally, through the integration of the Comb function, as defined in Equation 7:

$$\begin{aligned} \text{Comb}(x, A) &= C + \text{PW-Conv}(DW\text{-Conv}_3(C)) \\ \text{where } C &= x \otimes (1 + A) \end{aligned} \quad (7)$$

where $DW\text{-Conv}_3$ is the $3 \times 3 \times 3$ convolution block, we obtain the final output.

2.3.2 OmniFocus Attention Block

This block is at the deepest level of our network architecture, which has the most feature layers among all hybrid blocks. It works both residually in the encoder stage and collectively in the decoder stage. This block helps the model better capture important features while reducing noise. It does this by working with the convolutional information flow to improve feature representation. We use ViT channel attention along with LKAd in this block. This helps the model understand the connections between different channels using combined attention mechanisms, making it easier to transfer features to the next decoder layers. We also use the LKAd block in this block, similar to the Self-Adaptive Contextual Fusion Module, along with channel attention mechanisms. This combination helps the model address relationships between channels and long-range dependencies, allowing it to extract detailed feature representations. By integrating these mechanisms, the channel attention block allows the model to extract and use rich contextual information effectively, improving overall performance.

As depicted in Figure 2, the final output of this attention block similar to Equation (8) is computed as:

$$F_S = \text{Comb}(F, \delta_c \text{LKAd}(F) + \gamma_c \text{CA}(F)) \quad (8)$$

Where F denotes the previously extracted input feature maps in the shape of C, H, W, D and θ_c and γ_c represent learnable parameters per channel layers that control the combination weights of the two different attention mechanisms with respect to each head (h). The LKAd module computes attention to the input feature F following the formulation introduced in Equation (5), while CA denotes the channel attention module. This module examines the relationships between feature channels using a dot product operation between the channel value layer and the channel attention maps. Similar to the creation of Q , K , and V projections using three linear layers for self-attention, resulting in dimensions $n, h, C/h$, we repeat this process to obtain Q_C , K_C , and V_C for calculating channel attention:

$$x_{CA} = V_C \cdot \sigma \left(\frac{Q_C^T K_C}{\sqrt{d}} \right) \quad (9)$$

Next, x_{CA} goes through a linear normalization followed by a linear layer to enhance performance, similar to the result of the CA module. Then, as defined in Equation (7), using the given input x and the summation of weighted attention results, we generate the final output utilizing the Comb function.

3 Experimental setup and analysis

In this section, we discuss datasets, experimental setup, and evaluation matrices, used to showcase the effectiveness of our proposed framework for medical image segmentation.

3.1 Datasets

MICCAI Multi-Atlas Abdomen Labeling Challenge (Synapse) (Landman et al. 2015): The Synapse dataset consists of 30 abdominal CT scans ranging in size from $512 \times 512 \times 85$ to $512 \times 512 \times 198$ voxels. This collection offers a wide range of slice thicknesses (2.5 mm to 5.0 mm) and in-plane resolutions ($0.54 \times 0.54 \text{ mm}^2$ to $0.98 \times 0.98 \text{ mm}^2$), making it ideal for developing and testing advanced 3D segmentation algorithms. Following the method described in (Azad et al. 2024, Shaker et al. 2024), the training set of the dataset consists of 18 samples, with the remaining 12 samples reserved for testing. Each scan in this dataset is precisely labeled to identify eight major abdominal organs: the aorta, gallbladder, spleen, left and right kidneys, liver, pancreas, and stomach. The images were randomly cropped to $128 \times 128 \times 64$ for model input, as described in (Zhou et al. 2023, Isensee et al. 2021). The same method as in previous studies (Zhou et al. 2023, Chen et al. 2023) was used for inference.

Automated Cardiac Diagnosis Challenge (ACDC) (Bernard et al. 2018): The ACDC dataset, specifically designed to advance 3D cardiac image segmentation, consists of a collection of cine MRI images from a diverse group of 100 patients. This dataset is crucial for the advancement of advanced 3D segmentation algorithms, specifically in the accurate delineation of three major cardiac anatomical structures: the left ventricle (LV), the right ventricle (RV), and the myocardium (Myo). Each scan in this dataset provides intricate visual representations of these structures, allowing for extremely precise segmentation. The MRI scans vary in spatial resolution, typically ranging from 1.37 to 1.68 mm^2 per pixel. Furthermore, the dataset consists primarily of images with a slice thickness of 5 mm, while there are some occurrences with a slice thickness of 8 mm thickness. Occasionally, there is a 5 mm gap between slices. The variance in the thickness and the gaps between slices present specific obstacles for segmentation algorithms. These challenges require the use of strong approaches that can successfully handle these differences.

In terms of preprocessing, the method adheres to the protocols established in (Chen et al. 2023, Shaker et al. 2024), involving the random cropping of images to dimensions of $160 \times 160 \times 16$ and using sliding windows for the inference. The patient dataset is partitioned into separate subsets for the purpose of model training and evaluation. Specifically, 70 patients are assigned for training, 10 for validation, and 20 for testing. This allocation ensures a thorough evaluation of the segmentation models that are generated using the ACDC dataset.

Left Atrial Dataset (LA) (Xiong et al. 2021): constitutes a curated set of 100 three-dimensional MR images, all of which have undergone gadolinium enhancement. These images are uniform in resolution, each measuring 0.625 mm across all three spatial dimensions, with two prevalent spatial configurations: $640 \times 640 \times 88$ and $576 \times 576 \times 88$ pixels. The dataset has been divided into five distinct groups, with each group consisting of 20 patients. During the preprocessing stage, we followed the preprocessing in (Luo et al. 2021, Wang et al. 2023b) where the images are standardized to a zero mean and unit variance to facilitate consistent model input. The images also undergo strategic cropping, incorporating augmented margins to ensure the focal region is accentuated. During model training, random cropping of the volumes is performed to yield sub-volumes of $96 \times 96 \times 96$, which serve as inputs for the model. During the inference step, The study followed the methods outlined by (Wang et al. 2023b) utilizing the sliding window technique provided by the MONAI framework (Cardoso et al. 2022).

NIH pancreas dataset (CT-82) (Roth et al. 2015): This dataset encompasses a collection of 82 publicly available, contrast-enhanced, annotated three-dimensional CT scans of the abdominal region. Each scan within this dataset is characterized by a resolution of 512×512 pixels across the axial plane, with a variable number of slices spanning from 181 to 466 to accommodate the diverse anatomical structures present in the patient population. For structured analysis, the dataset is organized into four cohorts, with each segment comprising 20, 20, 21, and 21 patients, respectively. In alignment with the preprocessing methods proposed by (Luo et al. 2021, Wang et al. 2023b), this dataset underwent a standardized preprocessing protocol. The same configurations for training and inference as established for the LA dataset were applied.

Brain Tumor Segmentation (BraTS) Challenge 2018 (Bakas et al. 2017, Menze et al. 2014): The Brain Tumor Segmentation (BraTS) Challenge datasets from the year 2018 play a pivotal role in advancing medical image analysis. This dataset, constituting a diverse array of pre-operative Magnetic Resonance Imaging (MRI) scans, are sourced from

Table 2: Configuration specifics for network training across various datasets, highlighting the tailored approach to optimize performance for each unique dataset challenge.

	Synapse	ACDC	BraTS 2018	LA & Pancreas
Patch size	128 x 128 x 64	160 x 160 x 16	128 x 128 x 128	96 x 96 x 96
Base learning rate	0.003	0.003	0.01	0.01
Batch size	2	4	2	2
Sliding window overlap (%)	50	50	50	85
Downsample²	[2, 2, 1], 2, 2, 2, 2	[2, 2, 1], [2, 2, 1], [2, 2, 1], 2, 2	2, 2, 2, 2, 2	2, 2, 2, 2, 2

a multitude of institutions. Key characteristics of these datasets include the rigorous alignment of the MRIs, isotropic resampling to a resolution of $1 \times 1 \times 1$ mm, and the removal of the skull (skull-stripping). The MRIs present a uniform size of $240 \times 240 \times 155$. The data, encompassing a broad spectrum, are collected from several academic centers using varied MRI scanning equipment. Each dataset encompasses four MRI modalities: native T1, post-contrast T1-weighted (T1c), T2-weighted (T2), and T2 Fluid-attenuated Inversion Recovery (FLAIR). Tumor segmentation in these datasets is categorized into three distinct sub-regions: the Whole Tumor (WT), the Tumor Core (TC), and the Enhancing Tumor (ET). Prior to model training and analysis, this dataset underwent a standardized preprocessing method, following the preprocessing guideline proposed by (Dorent et al. 2019). For the training phase, MRI scans were randomly cropped to a size of $128 \times 128 \times 128$ voxels to fit the network input. During the inference phase, we employed MONAI’s (Cardoso et al. 2022) sliding window technique.

The BraTS-2018 dataset includes MRIs from 285 patients, with 210 exhibiting high-grade gliomas and 75 displaying low-grade gliomas. The data allocation was as follows: 70% for training, 10% for validation, and 20% for testing. The 2018 BraTS datasets provide an unparalleled resource for the advancement of automated brain tumor segmentation techniques, presenting diverse challenges and opportunities for the development of cutting-edge image analysis methods.

3.2 Experimental setup

The developed neural network model is implemented using Python (version 3.10.12) and is built upon the PyTorch framework (Paszke et al. 2019, Falcon and The PyTorch Lightning team 2019) (version 2.1.0). The model was trained on a single NVIDIA A100 graphics processing unit, equipped with 80 GB of VRAM. The training leveraged a composite loss function, DICE loss (Milletari et al. 2016) with binary cross-entropy, expressed as:

$$\mathcal{L}_{total} = 0.5 \cdot \mathcal{L}_{dice} + 0.5 \cdot \mathcal{L}_{ce} \quad (10)$$

In terms of optimization, we have utilized the Stochastic Gradient Descent (SGD) optimization method. The SGD configuration includes a weight decay factor of 3×10^{-5} , and a momentum of 0.99, enhanced with Nesterov momentum and a varied learning rate for each dataset. The learning rate is dynamically updated at each epoch following the equation:

$$\text{learning rate} = \text{base } lr \times \left(\frac{\text{epoch}}{\text{max_epoch}} \right)^{0.9} \quad (11)$$

Data augmentation techniques consistent with (Zhou et al. 2023, Shaker et al. 2024) were employed. The training duration differed across datasets. For the Synapse and ACDC datasets, the training involved 1000 epochs with 250 patches per epoch, resulting in a total of 250,000 iterations. For the BraTS dataset, we also used 1000 epochs. However, for the LA and Pancreas datasets, training consisted of 10,000 iterations. Table 2 summarizes the network configurations used for each dataset, detailing parameters such as patch size, initial learning rate, batch size, percentage of sliding window overlap, and downsampling strategy. These settings highlight the tailored approach to each dataset, aiming to optimize both performance and computational efficiency.

3.3 Evaluation metrics

Dice Similarity Coefficient (DSC) (Milletari et al. 2016): It is used to quantify the similarity between the predicted segmentation and the ground truth in medical images, formulated as below:

$$\text{DSC} = \frac{2 \times |\text{GT} \cap \text{PR}|}{|\text{GT}| + |\text{PR}|} \quad (12)$$

²A single integer indicates uniform downsampling across all axes.

where GT represents the ground truth segmentation, PR is the predicted segmentation, and $|\text{GT} \cap \text{PR}|$ is the number of pixels or voxels common to both.

Jaccard Similarity Coefficient (Taha and Hanbury 2015): This coefficient, also referred to as Intersection over Union, measures the overlap between the predicted segmentation and ground truth. It is calculated as:

$$\text{Jaccard Index} = \frac{|\text{GT} \cap \text{PR}|}{|\text{GT} \cup \text{PR}|} \quad (13)$$

where $|\text{GT} \cup \text{PR}|$ represents the total number of unique pixels or voxels in either the ground truth or the prediction.

95% Hausdorff Distance (HD95) (Taha and Hanbury 2015): It is a metric employed to assess the discrepancy between two point sets, commonly representing the ground truth and the predicted segmentation in image segmentation tasks. Contrary to the traditional Hausdorff Distance, which identifies the maximum distance among the sets, HD95 concentrates on the 95th percentile of these distances to minimize the effect of outliers. Formally, HD95 is delineated as the maximum of two directional distances at the 95th percentile:

$$\text{HD95}(\text{GT}, \text{PR}) = \max \left(\tilde{h}_{95}(\text{GT}, \text{PR}), \tilde{h}_{95}(\text{PR}, \text{GT}) \right) \quad (14)$$

where $\tilde{h}_{95}(\text{GT}, \text{PR})$ signifies the 95th percentile of all distances from points in the ground truth set to their nearest counterparts in the prediction set, and $\tilde{h}_{95}(\text{PR}, \text{GT})$ indicates the 95th percentile of distances for the inverse relation, from points in PR to their closest points in GT. metric focuses on the closest 95% of points between predicted and actual segmentations, excluding the most extreme 5% to reduce outlier impact. This provides a reliable gauge of segmentation accuracy, reflecting true model performance.

Average Surface Distance (ASD) (Taha and Hanbury 2015): ASD measures the average distance from points on the predicted segmentation surface to the closest points on the ground truth surface, and vice versa. The formula is:

$$\text{ASD}(\text{GT}, \text{PR}) = \frac{1}{|S_{\text{GT}}| + |S_{\text{PR}}|} \times \left(\sum_{g \in S_{\text{GT}}} \min_{p \in S_{\text{PR}}} d(g, p) + \sum_{p \in S_{\text{PR}}} \min_{g \in S_{\text{GT}}} d(p, g) \right) \quad (15)$$

where S_{GT} and S_{PR} are the surfaces of the ground truth and prediction, respectively, and $d(g, p)$ is the Euclidean distance between points g and p .

4 Results and Discussion

4.1 Quantitative Results and Discussion

MICCAI Multi-Atlas Abdomen Labeling Challenge (Synapse): Table 3 presents a comprehensive comparison of the LHU-Net model against leading models in the field on the Synapse dataset, a part of the MICCAI Multi-Atlas Abdomen Labeling Challenge. LHU-Net achieves an overall average DSC of 87.49%, demonstrating its strong performance in organ segmentation. Although LHU-Net and D-LKA Net have similar DSC scores, LHU-Net excels with a better HD95 metric. LHU-Net maintains high accuracy with a model size of only 10.52 million parameters and requires 51.75 billion FLOPS, showing a good balance between performance and efficiency. This is particularly notable compared to many 2D state-of-the-art models, which usually have fewer parameters. LHU-Net leads in spleen segmentation with a DSC of 96.01%, evidencing its capability in accurately delineating this organ. It also achieves notable success in segmenting the right kidney, with DSCs of 87.80% illustrating its adeptness in handling organs with complex anatomical structures. The model also performs well in segmenting the gallbladder and liver, organs known for their challenging variability in shape and size, with DSCs of 72.42% and 96.68%, respectively. This is particularly significant given the gallbladder’s propensity for variable positioning and the liver’s large spatial occupancy, further emphasizing LHU-Net’s robust feature extraction capabilities. A key strength of LHU-Net is its achievement of the lowest HD95 across all models at 4.15 mm. This indicates high precision, ensuring that 95% of the points on the predicted segmentation surface are within 4.15 mm of the actual surface. Such precision is crucial for clinical applications, where accurate segmentation impacts treatment planning and patient outcomes. Compared to other high-performance models, LHU-Net not only excels in segmentation accuracy but also in computational efficiency. It performs better than more computationally intensive models like TC-CoNet and Swin-UNETR, showing that increased model complexity does not always lead to better performance.

Automated Cardiac Diagnosis Challenge (ACDC): Table 4 provides a detailed comparative analysis of advanced deep learning models applied to the Automated Cardiac Diagnosis Challenge (ACDC) dataset, focusing on the segmentation

Table 3: Comparative analysis of our approach versus state-of-the-art in the benchmarks for MICCAI Multi-Atlas Abdomen Labeling Challenge (Synapse). The highest-performing result is highlighted in **blue**, while the second-best result is denoted in **red**. Parameter counts are reported in millions (M), and FLOPS are expressed in billions (G). The Dice Similarity Coefficient (DSC) for Spleen (Spl), Right Kidney (RKid), Left Kidney (LKid), Gallbladder (Gal), Liver (Liv), Stomach (Sto), Aorta (Aor), and Pancreas (Pan) are detailed as percentages. Furthermore, the average DSC and 95% Hausdorff Distance (HD95) for all organs are included to provide a comprehensive evaluation of segmentation accuracy. Two-dimensional (2D) models are indicated with *, and three-dimensional (3D) models are *italicized*.

Methods	Params↓	FLOPS↓	Spl	RKid	LKid	Gal	Liv	Sto	Aor	Pan	Average	
											DSC↑	HD95↓
U-Net* (Ronneberger et al. 2015)	-	-	86.67	68.60	77.77	69.72	93.43	75.58	89.07	53.98	76.85	-
TransUNet* (Chen et al. 2021)	96.07 M	88.91 G	85.08	77.02	81.87	63.16	94.08	75.62	87.23	55.86	77.49	31.69
SSTrans-Net* (Fu et al. 2024)	29.64 M	-	92.23	83.33	86.99	72.87	94.61	81.37	86.72	64.98	82.89	15.55
FET* (Azad et al. 2023c)	47.01 M	-	91.85	80.06	86.66	69.67	94.43	80.34	85.31	67.08	81.92	18.41
HiFormer* (Heidari et al. 2023)	25.51 M	-	90.99	79.77	85.23	65.69	94.61	81.08	86.21	59.52	80.39	14.70
UNETR (Hatamizadeh et al. 2022)	92.49 M	75.76 G	85.00	84.52	85.6	56.3	94.57	70.46	89.8	60.47	78.35	18.59
Swin-UNETR (Hatamizadeh et al. 2021)	62.83 M	384.2 G	95.37	86.26	86.99	66.54	95.72	77.01	91.12	68.8	83.48	10.55
nnFormer (Zhou et al. 2023)	150.5 M	213.4 G	90.51	86.25	86.57	70.17	96.84	86.83	92.04	83.35	86.57	10.63
UNETR++ (Shaker et al. 2024)	42.96 M	47.98 G	95.77	87.18	87.54	71.25	96.42	86.01	92.52	81.1	87.22	7.53
MoAFormer (Luo et al. 2022)	~ 50 M	-	92.21	85.23	86.72	71.84	95.92	81.56	89.73	75.46	84.80	16.3
TC-CoNet (Chen et al. 2023)	313.67 M	699.58 G	91.77	87.92	88.16	62.00	96.35	79.4	92.45	72.78	83.86	9.64
D-LKA Net (Azad et al. 2024)	42.35 M	66.96 G	95.88	88.50	87.64	72.14	96.25	85.03	92.87	81.64	87.49	9.57
MS-TCNet (Ao et al. 2024)	~ 59 M	~ 172 G	93.70	86.66	86.88	66.96	95.82	82.82	91.60	68.19	84.08	8.44
MOSformer (Huang et al. 2024)	~ 77 M	~ 100 G	92.29	83.58	90.32	71.90	95.96	87.87	88.95	74.14	85.63	13.4
HCA-former (Yang et al. 2024)	~ 100 M	-	92.46	86.67	87.21	70.19	96.52	85.91	92.65	82.24	86.92	7.86
LHU-Net	10.52 M	51.75 G	96.01	87.80	87.57	72.43	96.68	85.79	92.42	81.21	87.49	4.15

of key cardiac structures: the left ventricle (LV), myocardium (Myo), and right ventricle (RV). Using the DSC as the main metric, the LHU-Net model stands out with an average DSC of 92.66%, highlighting its effectiveness in segmenting cardiac structures. LHU-Net is highly efficient, with only 5.07 million parameters and the lowest computational footprint at 12.37 billion FLOPS. This efficiency contrasts with other models, which have higher parameters and computational demands but only small performance gains. LHU-Net’s design shows that significant performance improvements can be achieved without increasing computational demands. Notably, LHU-Net also has a lower parameter count compared to many 2D models, which usually have fewer parameters. LHU-Net performs exceptionally well in segmenting the myocardium (Myo) with a DSC of 90.56%, which is crucial given the Myo’s complex structure and importance in diagnostics. It also excels in LV and RV segmentation, with DSCs of 96.26% and 91.15%, respectively, matching or surpassing top models. Compared to other models like D-Former and MOSformer, which have good DSC scores but require more resources, LHU-Net is more efficient. For example, D-Former has an average DSC of 92.29% but uses significantly more resources, showing that higher model complexity does not always lead to better performance. LHU-Net achieves better performance with over 85% fewer parameters and nearly 70% less FLOPS compared to some models, proving that smart design can lead to excellent results without heavy computational costs.

Left Atrial Dataset (LA): Table 5 presents a detailed quantitative analysis of several methods. The LHU-Net model serves as a strong benchmark in the analysis of the Left Atrial Dataset. This model excels in standard metrics like DSC and Jaccard index and also sets high standards in ASD and HD95, showcasing its overall segmentation capability. With a lean architecture of just 8.57 million parameters and 34.28 billion FLOPS, LHU-Net is efficient and effective. It achieves an impressive average DSC of 91.55, slightly surpassing SwinUNETR-V2, demonstrating its ability to delineate the left atrium’s complex anatomy accurately. This slight edge in DSC is supported by strong performance in the Jaccard index at 84.54, reinforcing its effectiveness in capturing the true extent of atrial structures. Importantly, LHU-Net achieves the lowest scores in ASD (1.55) and HD95 (4.97). These scores indicate the model’s high precision in approximating the true surface of the atrium and minimizing the distance to the farthest outliers. This precision is crucial for clinical applications where every millimeter is important. The ASD score, in particular, highlights LHU-Net’s ability to match the actual atrial boundary across all dataset variations consistently. While other models like UNETR++ and SwinUNETR-V2 perform well, especially in 3D segmentation tasks, they do not balance high accuracy and computational efficiency as effectively as LHU-Net. For instance, despite SwinUNETR-V2’s competitive DSC and Jaccard scores, LHU-Net’s superior ASD and HD95 metrics show its ability to provide more reliable and precise segmentations, which are essential for clinical diagnostics and interventions.

NIH pancreas dataset (CT-82): Table 6 provides a quantitative assessment of various segmentation models on the NIH Pancreas dataset (CT-82). LHU-Net demonstrates strong performance across multiple metrics, including average DSC, HD95, Jaccard index, and ASD. With an efficient architecture requiring only 8.57 million parameters and 34.28 billion FLOPS, LHU-Net achieves an average DSC of 81.96 and the lowest HD95 at 6.78. This reflects its ability to accurately delineate pancreatic tissues, minimizing segmentation errors that are crucial in clinical diagnostics. The model also

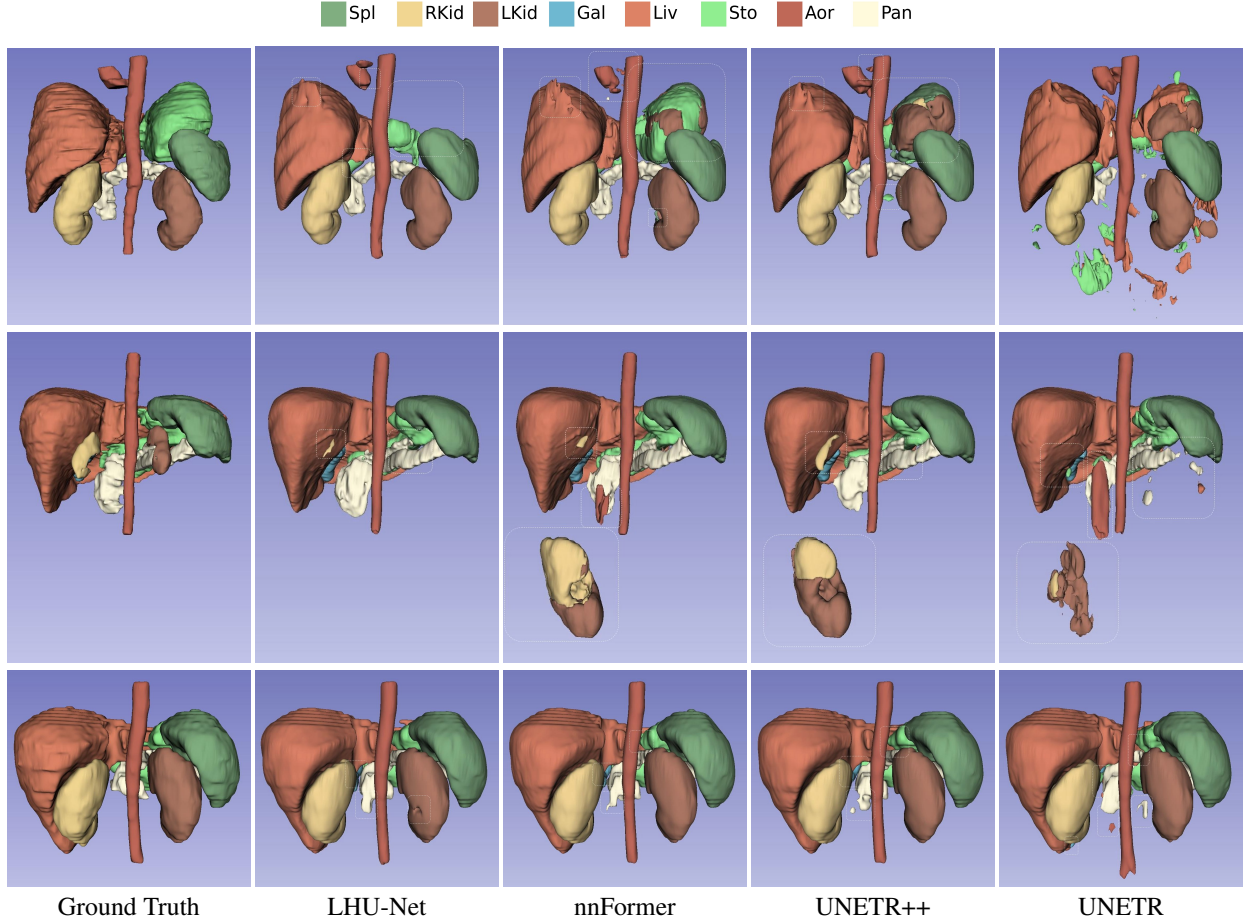


Figure 3: Qualitative comparison of the results of our model with respect to other state-of-the-art (SOTA) in MICCAI Multi-Atlas Abdomen Labeling Challenge (Synapse) (images were generated using 3D Slicer (Fedorov et al. 2012)).

performs well on the Jaccard index, with a leading score of 70.12, indicating a high overlap between the segmented and actual pancreatic regions. Additionally, LHU-Net’s ASD score of 1.31 shows its precision in approximating the surface of the pancreas, ensuring that the segmented boundary closely matches the true anatomical boundary. Unlike other models like UNETR++ and SwinUNETR-V2, LHU-Net offers a more computationally efficient framework without compromising segmentation accuracy. Its balance of optimizing computational resources and maintaining high segmentation fidelity makes LHU-Net a suitable choice for clinical use, where both time and computational efficiency are important. In summary, LHU-Net demonstrates high accuracy in DSC, HD95, Jaccard, and ASD metrics, along with computational efficiency.

Brain Tumor Segmentation (BraTS) Challenge 2018: Table 7 provides a detailed comparison of various deep learning models, showing their performance in terms of DSC and HD95 for the BraTS Challenge 2018 dataset. In this study, the LHU-Net model excels by achieving the highest average DSC and the lowest average HD95, indicating its effectiveness in accurately identifying tumor boundaries and regions. LHU-Net performs particularly well in segmenting ET and WT and excels in delineating the TC. This is achieved with a lower parameter count of 10.5 million and a reasonable computational demand, as shown by its FLOPS measurement. LHU-Net’s performance in segmenting the TC is noteworthy, achieving a DSC of 87.42, which is crucial due to the clinical importance of the TC as it contains the bulk of malignant tissue. In the WT category, representing the entire tumor area, LHU-Net leads with a DSC of 89.57, showing its ability to capture the full extent of the tumor. LHU-Net balances high accuracy with relatively low computational overhead. While the UNETR++ model shows competitive performance, especially in ET segmentation, LHU-Net’s consistent excellence across all tumor segmentation measures makes it a reliable model for comprehensive and accurate segmentations.

Table 4: Comparative analysis of our approach versus state-of-the-art in the benchmarks for Automated Cardiac Diagnosis Challenge (ACDC). The highest-performing result is highlighted in **blue**, while the second-best result is denoted in **red**. Parameter counts are reported in millions (M), and FLOPS are expressed in billions (G). Dice Similarity Coefficient (DSC) is provided for the Left Ventricle (LV), Right Ventricle (RV), and Myocardium (Myo), expressed as a percentage. Two-dimensional (2D) models are indicated with *, and three-dimensional (3D) models are *italicized*. The overall average DSC across all heart regions is also provided to reflect comprehensive model performance.

Methods	Params↓	FLOPS↓	LV	Myo	RV	Avg. DSC ↑
TransUNet* (Chen et al. 2021)	-	-	95.73	84.54	88.86	89.71
Swin-UNet* (Cao et al. 2022)	-	-	95.83	85.62	88.55	90.00
SSTrans-Net* (Fu et al. 2024)	29.64 M	-	94.40	87.51	89.02	90.31
<i>UNETR</i> (Hatamizadeh et al. 2022)	92.69 M	77.84 G	94.02	86.52	85.29	88.61
<i>nnFormer</i> (Zhou et al. 2023)	37.16 M	47.73 G	95.59	89.53	90.22	91.78
<i>MoFormer</i> (Luo et al. 2022)	46.12 M	-	95.15	88.49	90.15	91.26
<i>TC-CoNet</i> (Chen et al. 2023)	86.79 M	145.16 G	95.47	88.98	90.27	91.58
<i>D-LKA Net</i> (Azad et al. 2024)	39.95 M	42.41 G	94.68	88.04	91.35	91.36
<i>neU-Net</i> (Yang et al. 2023)	161.28 M	129.83 G	95.66	89.91	90.75	92.11
<i>HCA-Former</i> (Yang et al. 2024)	~ 100 M	-	95.8	89.76	90.77	92.11
<i>MOSformer</i> (Huang et al. 2024)	77.09 M	100.06 G	96.05	89.65	90.86	92.19
<i>MS-TCNet</i> (Ao et al. 2024)	59.49 M	172.89 G	95.77	89.09	89.43	91.43
<i>D-Former</i> (Wu et al. 2023)	~ 40 M	~ 50 G	95.93	89.60	91.33	92.29
LHU-Net	5.07 M	12.37 G	96.26	90.56	91.15	92.66

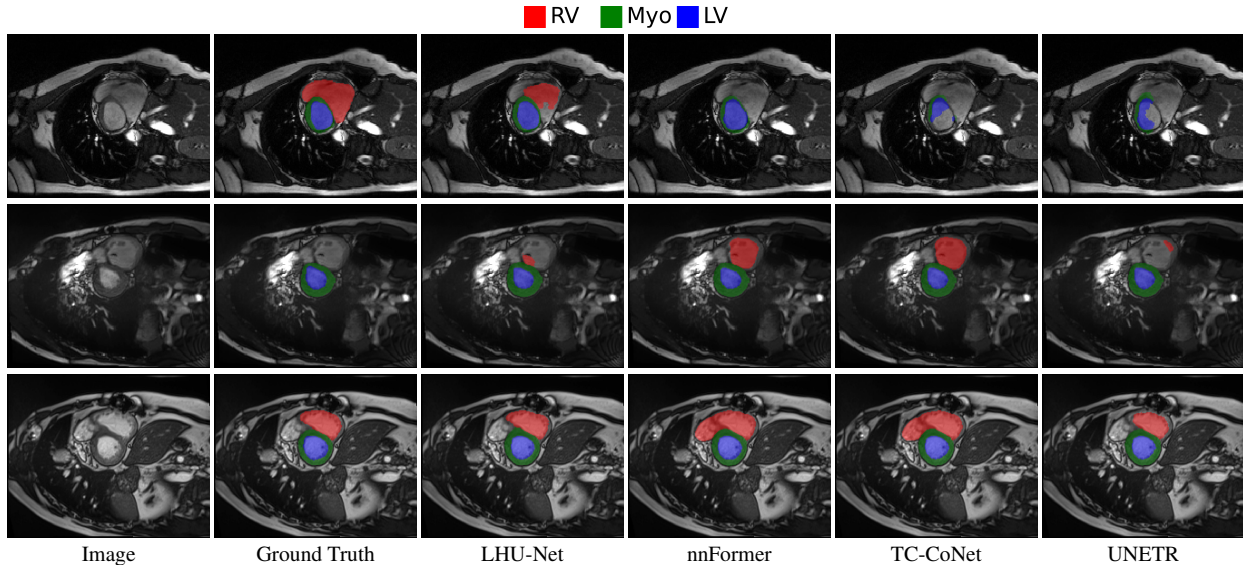


Figure 4: Qualitative comparison of the results of our model with respect to other SOTA in Automated Cardiac Diagnosis Challenge (ACDC) dataset.

4.2 Qualitative Results and Discussion

Following the quantitative analysis, we shift our focus to a qualitative evaluation of the same datasets. We assess the models’ performance through visual examination, considering details that numerical data may miss. This section describes how well the models’ segmentations match the expected outcomes and the ground truth in the medical images. This qualitative view gives us insights into the models’ practical capabilities and their potential for clinical use.

MICCAI Multi-Atlas Abdomen Labeling Challenge (Synapse): Figure 3 offers a qualitative perspective on the segmentation capabilities of various models in the MICCAI Multi-Atlas Abdomen Labeling Challenge (Synapse). For the first patient, shown in the top row, UNETR produces fragmented and scattered segmentations that do not accurately

Table 5: Comparative analysis of our approach versus state-of-the-art in the benchmarks for Left Atrial Dataset (LA). The top-performing result is highlighted in **blue**, while the next best is marked in **red**. A five-fold cross-validation approach has been employed, and the results are displayed as mean followed by standard deviation across all folds. Parameter counts are reported in millions (M), and FLOPS are expressed in billions (G). DSC and Jaccard metrics are reported in percentages.

Methods	Params↓	FLOPS↓	Average			
			ASD ↓	DSC ↑	HD95 ↓	Jaccard ↑
SwinUNETR (Hatamizadeh et al. 2021)	62.2 M	319.38 G	1.90 (0.34)	91.20 (1.07)	6.07 (1.16)	83.92 (1.57)
SwinUNETR-V2 (He et al. 2023)	72.77 M	345.23 G	1.74 (0.28)	91.48 (0.79)	5.59 (1.03)	84.41 (1.26)
UNETR (Hatamizadeh et al. 2022)	92.78 M	73.51 G	3.60 (0.47)	88.25 (1.31)	11.55 (1.58)	79.32 (1.97)
UNETR++ (Shaker et al. 2024)	29.54 M	29.74 G	1.77 (0.30)	91.05 (1.12)	5.47 (1.01)	83.62 (1.79)
nnFormer (Zhou et al. 2023)	149.25 M	176.45 G	2.49 (0.36)	88.79 (1.98)	7.09 (0.75)	80.21 (2.72)
VNet (Milletari et al. 2016)	9.44 M	82.76 G	1.99 (0.31)	89.90 (1.79)	6.11 (1.09)	81.91 (2.65)
LHU-Net	8.55 M	32.55 G	1.55 (0.14)	91.55 (0.95)	4.97 (0.75)	84.54 (1.51)

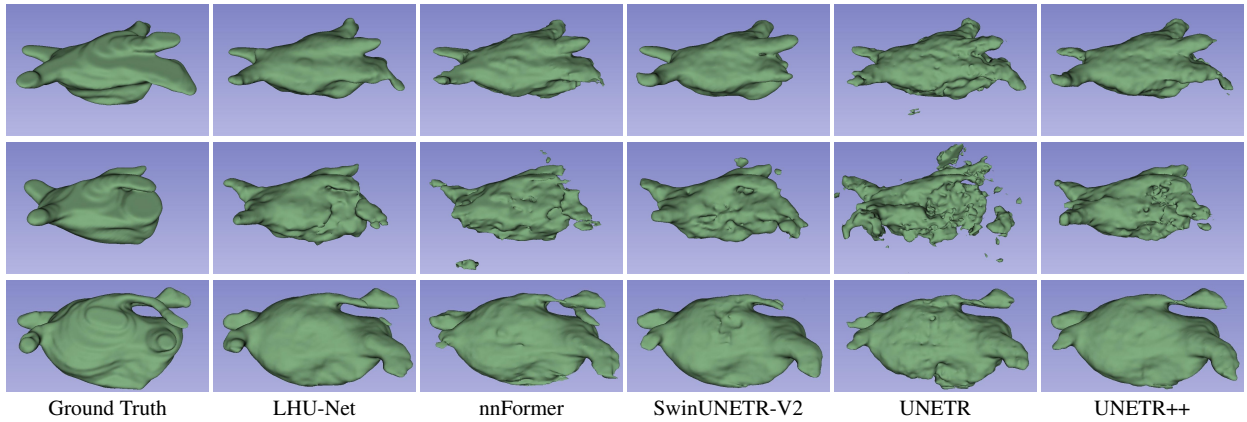


Figure 5: Qualitative comparison of the results of our model with respect to other SOTA in Left Atrial Dataset (images were generated using 3D Slicer (Fedorov et al. 2012)).

represent the organs. nnFormer and UNETR++ have irregular segmentation contours, especially for the left kidney and aorta, with UNETR++ also missing the stomach. In contrast, the LHU-Net model performs well, accurately delineating most organs with smooth boundaries, although it slightly overestimates the aorta. These smooth boundaries reflect the low HD95 observed in the quantitative results. The middle row shows the second patient, presenting a more challenging scenario. All models struggle, particularly with kidney segmentation. nnFormer and UNETR++ detect large areas far from the ground truth, highlighting the importance of minimizing false positives. LHU-Net performs better by correctly segmenting most organs, with only minor inaccuracies in the kidneys, indicating a better understanding of organ boundaries. For the third patient, depicted in the bottom row, the pancreas is particularly challenging to segment, complicated by the absence of the gallbladder in the ground truth. LHU-Net precisely delineates the organ boundaries, while UNETR++ and nnFormer struggle with the pancreas’s tail and its edges. UNETR continues to have issues with segmentation accuracy across multiple organs, including the aorta. All models mistakenly predict the presence of the gallbladder, highlighting a common challenge in identifying missing organs. In conclusion, the LHU-Net model shows strong performance in organ detection and segmentation across the Synapse dataset. Its results are smoother and more accurate, with better resistance to false positives, which is crucial for clinical applications. The smooth boundaries achieved by LHU-Net align with the low HD95 seen in the quantitative results, reinforcing its precision in medical image segmentation.

Automated Cardiac Diagnosis Challenge (ACDC): Figure 4 provides a qualitative, two-dimensional evaluation of cardiac segmentation across several advanced models using the ACDC dataset. This visual assessment covers three different patient cases, each represented by a distinct row of images, to compare how well each model segments the left ventricle (LV), myocardium (Myo), and right ventricle (RV). For the first patient, shown in the top row, all models struggle with segmenting the RV. LHU-Net partially captures this structure, while TC-CoNet and UNETR show difficulties in accurately delineating the Myo and LV, as seen by their deviations from the ground truth. In the second patient, depicted in the middle row, the absence of the RV in the slice tests the models’ specificity. Here, LHU-Net

Table 6: Comparative analysis of our approach versus state-of-the-art in the benchmarks for NIH pancreas dataset (CT-82). The top-performing result is highlighted in **blue**, while the next best is marked in **red**. A four-fold cross-validation approach has been employed, and the results are displayed as mean followed by standard deviation across all folds. Parameter counts are reported in millions (M), and FLOPS are expressed in billions (G). DSC and Jaccard metrics are reported in percentages.

Methods	Params↓	FLOPS↓	Average			
			ASD↓	DSC↑	HD95↓	Jaccard↑
SwinUNETR (Hatamizadeh et al. 2021)	62.2 M	319.38 G	1.99 (0.51)	80.52 (2.13)	7.52 (1.52)	68.17 (2.79)
SwinUNETR-V2 (He et al. 2023)	72.77 M	345.23 G	2.42 (0.97)	81.05 (1.90)	8.85 (2.55)	68.87 (2.52)
UNETR (Hatamizadeh et al. 2022)	92.78 M	73.51 G	4.25 (0.83)	76.18 (2.55)	12.98 (2.50)	62.51 (3.24)
UNETR++ (Shaker et al. 2024)	29.54 M	29.74 G	1.95 (0.22)	81.49 (0.84)	7.64 (2.01)	69.07 (1.16)
nnFormer (Zhou et al. 2023)	149.25 M	176.45 G	3.28 (0.90)	78.05 (2.29)	10.65 (3.74)	64.81 (2.81)
VNet (Milletari et al. 2016)	9.44 M	82.76 G	2.79 (0.30)	79.31 (1.95)	8.99 (1.96)	66.42 (2.55)
LHU-Net	8.55 M	32.55 G	1.31 (0.14)	81.96 (1.00)	6.78 (0.52)	70.12 (1.29)

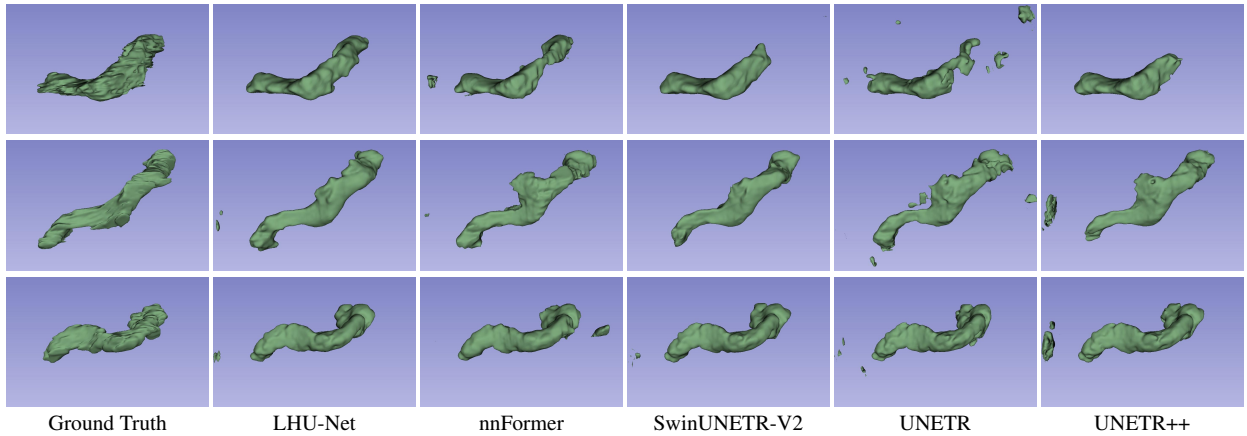


Figure 6: Qualitative comparison of the results of our model with respect to other SOTA in NIH pancreas dataset (images were generated using 3D Slicer (Fedorov et al. 2012)).

avoids overprediction, which is a problem seen in nnFormer and TC-CoNet, as they incorrectly identify a substantial RV presence. All models perform well in segmenting the Myo and LV under these conditions. For the third patient, shown in the bottom row, LHU-Net’s segmentation closely matches the ground truth, effectively capturing all relevant cardiac structures. In contrast, nnFormer and TC-CoNet tend to over-segment the RV, while UNETR under-segments it, indicating potential limitations in their algorithms. In conclusion, the visual assessment suggests that LHU-Net has strong robustness and precision in segmenting cardiac structures, performing better than the other models in various conditions. This robustness is especially evident in avoiding false positives and accurately delineating challenging structures like the RV.

Left Atrial Dataset (LA): Figure 5 provides a qualitative, three-dimensional visualization of various models’ performance in segmenting the Left Atrial dataset for individual patients. Each row in the figure shows the segmentation results from a single patient’s dataset, visually assessing each model’s predictive capabilities. For the first patient, shown in the top row, all models except UNETR manage to generate a single entity segmentation, highlighting their ability to integrate anatomical features into a unified model prediction. However, all models struggle with accurately segmenting the right corner of the atrium, indicating an area for improvement. For the second patient, shown in the middle row, many models struggle to segment the ground truth accurately, resulting in multiple segmented instances rather than a single cohesive structure. In contrast, LHU-Net produces a single, continuous segmentation that closely resembles the ground truth, demonstrating its ability to generate smoother and more coherent segmentations. For the third patient, depicted in the bottom row, all models show a tendency for over-segmentation at the base of the atrium, reflecting the complexity of accurately delineating this region. Additionally, some models, specifically UNETR and SwinUNETR-V2, also exhibit under-segmentation in other areas, adding to the segmentation challenge. In summation, the visualizations in Figure 5 suggest that LHU-Net consistently generates more robust and smoother segmentations, avoiding the creation of extraneous entities.

Table 7: Comparative analysis of our approach versus state-of-the-art in the benchmarks for Brain Tumor Segmentation (BraTS) Challenge 2018. The top-performing result is highlighted in **blue**, while the next best is marked in **red**. Parameter counts are reported in millions (M), and FLOPS are expressed in billions (G). The terms "Whole Tumor" (WT) refer to the entire tumor area, "Tumor Core" (TC) denotes the central region of the tumor, and "Enhancing Tumor" (ET) highlights areas with active tumor cells that are visible after contrast enhancement.

Methods	Params	FLOPS	DSC \uparrow			HD95 \downarrow			Average	
			ET	TC	WT	ET	TC	WT	DSC \uparrow	HD95 \downarrow
ResUNet (Lee et al. 2017)	28.44 M	472.62 G	78.6	82.74	88.75	6.519	9.886	9.547	83.36	8.651
ResUNetSE (Toubal et al. 2020)	29.31 M	472.8 G	77.84	82.55	88.67	6.699	8.954	8.066	83.02	7.906
3D-UNET (Çiçek et al. 2016)	16.47 M	516.71 G	78.02	82.99	88.92	7.103	9.884	8.228	83.31	8.405
SwinUNETR-V2 (He et al. 2023)	72.77 M	836.26 G	80.75	84.15	88.04	5.591	7.807	7.84	84.31	7.079
SwinUNETR (Hatamizadeh et al. 2021)	62.2 M	774.98 G	79.43	82.39	88.51	5.835	7.625	10.87	83.44	8.11
UNETR (Hatamizadeh et al. 2022)	102.45 M	184.76 G	76.97	78.81	86.51	9.182	11.48	13.44	80.76	11.367
UNETR++ (Shaker et al. 2024)	42.65 M	73.59 G	82.29	85.87	89.38	4.348	6.456	6.23	85.85	5.678
nnFormer (Zhou et al. 2023)	37.75 M	106.45 G	78.95	85.57	89.4	5.676	6.362	8.723	84.64	6.920
LHU-Net	10.50 M	81.96 G	81.16	87.42	89.57	3.779	5.632	6.481	86.05	5.597

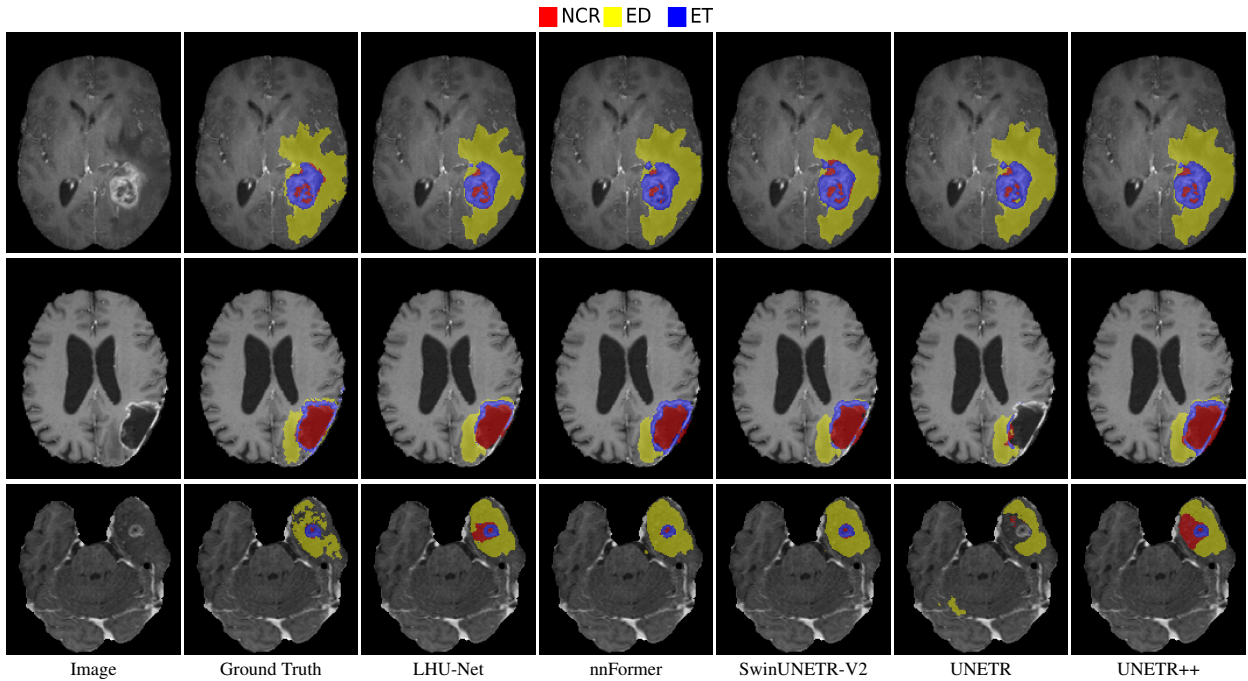


Figure 7: Qualitative comparison of the results of our model with respect to other SOTA in Brain Tumor Segmentation (BraTS) Challenge 2018 dataset.

NIH pancreas dataset (CT-82): Figure 6 provides a three-dimensional visualization for the qualitative analysis of pancreatic segmentation across several advanced models. Each row shows the segmentation results from an individual patient's dataset, giving insight into the predictive accuracy of each model. For the first patient, shown in the top row, all models except LHU-Net, UNETR++, and SwinUNETR-v2 fail to produce a singular, cohesive entity representing the pancreas. UNETR++ generates a single entity but significantly under-segments the pancreas, missing parts of the anatomical structure. In contrast, LHU-Net achieves a segmentation that closely matches the ground truth, highlighting its ability to preserve the organ's integrity. The second patient's data, depicted in the middle row, further demonstrates LHU-Net's proficiency in producing smooth and robust segmentation compared to other models. Notably, UNETR++ shows fragmentation in the segmentation, resulting in multiple entities, indicating a lack of robustness. For the third patient, shown in the bottom row, all models struggle with the dataset, predicting multiple entities. However, LHU-Net stands out by accurately segmenting the main portion of the pancreas that aligns with the ground truth and generating only a minor secondary entity. This contrasts with other models, which produce multiple, larger erroneous segments, compromising the segmentation's accuracy. Overall, LHU-Net demonstrates greater robustness and smoothness in its segmentation outputs, consistently predicting the pancreas with higher anatomical accuracy.

Brain Tumor Segmentation (BraTS) Challenge 2018: Figure 7 provides a qualitative comparison of segmentation results on the Brain Tumor Segmentation (BraTS) Challenge 2018 dataset, showing the performance of the LHU-Net model relative to other advanced models. Each row in the figure corresponds to a different patient’s MRI slice, highlighting the segmentation of three tumor regions: the necrotic and non-enhancing tumor core (NCR), the peritumoral edematous/invaded tissue (ED), and the enhancing tumor (ET). These regions are important for evaluating the extent and severity of brain tumors. For the first patient, shown in the top row, the models face challenges in distinguishing between NCR and ET. While many models can segment the whole tumor (WT) and tumor core (TC), identifying ET from NCR is more difficult. LHU-Net, while generally accurate, shows some difficulties at the boundaries of the NCR. SwinUNETR-V2 attempts to delineate the NCR at the edges, but with some misplaced detections, highlighting the complexity of this task. Overall, LHU-Net provides more robust and smoother segmentations, indicating its advanced capability in differentiating within tumor regions. The second patient, shown in the middle row, has a large NCR with a smaller ET region around it. LHU-Net accurately delineates all regions, while models like UNETR struggle with the finer details of the NCR and ET. Other models tend to overestimate the size of the NCR, demonstrating the difficulty in capturing precise tumor boundaries. LHU-Net’s performance here underscores its capability to segment with precision, even in complex scenarios. For the third patient, shown in the bottom row, the small NCR and ET within the irregularly shaped ED tissue present a significant challenge. Most models, including UNETR, produce a continuous segmentation of the ED but also show additional entities far from the tumor’s actual location, indicating false positives. In contrast, UNETR++ and LHU-Net tend to over-segment the NCR, while SwinUNETR-V2 and nnFormer strive to provide complete segmentation across all regions, despite the difficult nature of the task.

5 Ablation studies

This section examines the detailed structure of our LHU-Net model. We look closely at the different types of macro CNN and hybrid modules, how repeating hybrid modules affect the model, and the role of different attention mechanisms. These studies are important to see how each part of the model affects its performance.

Influence of macro module composition: The LHU-Net model uses a mix of convolutional neural networks (CNN) and hybrid macro modules arranged to extract optimal features. We study how the model’s performance changes when we alter the network depth by changing the number of downsampling stages and the types of macro modules at each level. In Table 8, we show how changing the number of macro modules affects the DSC on the ACDC dataset. As explained in Section 2, our setup starts with CNN modules followed by hybrid modules. We found that reducing the downsampling layers from five to four cuts down the number of parameters, but it also lowers the DSC, indicating a trade-off between model complexity and segmentation accuracy. We also found that just adding more CNN macro modules does not improve performance. This shows that having too many of these modules does not lead to better results. The best setup for our LHU-Net, which is the proposed model configuration, has two CNN macro modules followed by three hybrid macro modules. This setup achieves the highest DSC, showing the need for a balanced macro-module arrangement for effective segmentation tasks.

Table 8: Ablation analysis on the effects of macro module composition on the ACDC dataset performance, evaluated using the average DSC. The optimal model configuration is highlighted in **bold**.

N. CNNs	N. hybrids	Params	Avg. DSC ↑
2	2	3.37 M	92.43
2	3	5.07 M	92.66
3	2	3.07 M	92.31

Influence of number of repetitions in hybrid macro modules: In the hybrid module of LHU-Net, we can repeat the same block in each layer. Table 9 presents the impact of repeating the hybrid macro block on the ACDC dataset. Using just one repetition of the hybrid module in each layer, as shown in Table 9, results in lower computational complexity and fewer parameters, which also yields the best performance with an average DSC of 92.66. More repetitions increase the computational demand but do not effectively capture the unique features needed at each level. This is likely because repeating the same module multiple times may lead to redundancy and fail to identify distinct features specific to each layer. Thus, increasing the number of repetitions does not always improve performance. By carefully selecting and using a single repetition of the hybrid modules in LHU-Net, we were able to achieve better results. This highlights the importance of a balanced approach in designing neural network architectures, where adding more layers or repetitions does not necessarily translate to better performance. Instead, focusing on the quality and specific role of each module can lead to more efficient and effective models.

Table 9: Ablation analysis on the effects of the number of repetitions in hybrid macro modules on the ACDC dataset performance, evaluated using the average DSC. The optimal model configuration is highlighted in **bold**.

Hybrid modules repetition	Params	Avg. DSC \uparrow
1	5.07 M	92.66
2	9.09 M	92.41
3	13.11 M	91.51

Influence of attention mechanisms within hybrid macro modules: In the hybrid macro modules of LHU-Net, we can use different types of attention blocks, like OmniFocus attention and self-adaptive contextual fusion modules. OmniFocus attention boosts important features across channels, while the self-adaptive contextual fusion module focuses on relevant spatial information. Placing these blocks correctly within the hybrid macro modules is key to the model’s performance.

Our study looks at how different configurations of these attention blocks affect the average DSC on the ACDC dataset. Table 10 shows the results of this analysis. The best sequence of hybrid blocks is two self-adaptive contextual fusion modules followed by an OmniFocus attention block. This setup gave the highest average DSC, showing better segmentation when spatial attention is used early on. This is because it captures the important spatial features well. The channel attention then refines these features across the channels, highlighting the need for a varied but well-planned arrangement of attention mechanisms.

Table 10: Ablation analysis investigating the impact of attention block sequence within hybrid macro modules on segmentation performance in the ACDC dataset. *S* represents self-adaptive contextual fusion module, and *C* represents OmniFocus attention. The most effective sequence is highlighted in **bold**.

Sequence of attentions	Avg. DSC \uparrow
SSS	92.32
CCC	92.24
SSC	92.66
SCC	92.5

Our study shows that the choice of attention blocks within the hybrid modules is not just a matter of preference. It is an important decision that greatly affects the model’s performance.

6 Conclusion

In this work, we introduced LHU-Net, a novel light hybrid U-Net architecture tailored for volumetric medical image segmentation. LHU-Net effectively combines simple design with high performance through the strategic use of attention mechanisms. We integrate spatial attention in the initial layers to capture broad features and channel attention in deeper layers for precise feature refinement. This design allows LHU-Net to efficiently handle diverse datasets and various segmentation tasks with fewer than 11 million parameters. Our findings highlight that it is possible to achieve high segmentation accuracy with a less complex model. This marks a significant advancement in developing accessible and powerful medical image analysis tools, demonstrating the potential of LHU-Net in improving medical imaging practices.

Acknowledgment

The authors gratefully acknowledge the computational and data resources provided by the Leibniz Supercomputing Centre (www.lrz.de).

References

- Jonathan Long, Evan Shelhamer, and Trevor Darrell. Fully convolutional networks for semantic segmentation. In *Proceedings of the IEEE conference on computer vision and pattern recognition*, pages 3431–3440, 2015.
- Olaf Ronneberger, Philipp Fischer, and Thomas Brox. U-net: Convolutional networks for biomedical image segmentation. In *Medical Image Computing and Computer-Assisted Intervention–MICCAI 2015: 18th International Conference, Munich, Germany, October 5–9, 2015, Proceedings, Part III 18*, pages 234–241. Springer, 2015.
- Chen Liang-Chieh, George Papandreou, Iasonas Kokkinos, Kevin Murphy, and Alan Yuille. Semantic image segmentation with deep convolutional nets and fully connected crfs. In *International Conference on Learning Representations*, 2015.
- Kaiming He, Xiangyu Zhang, Shaoqing Ren, and Jian Sun. Deep residual learning for image recognition. In *Proceedings of the IEEE conference on computer vision and pattern recognition*, pages 770–778, 2016.
- Fausto Milletari, Nassir Navab, and Seyed-Ahmad Ahmadi. V-net: Fully convolutional neural networks for volumetric medical image segmentation. In *2016 fourth international conference on 3D vision (3DV)*, pages 565–571. Ieee, 2016.
- Reza Azad, Ehsan Khodapanah Aghdam, Amelie Rauland, Yiwei Jia, Atlas Haddadi Avval, Afshin Bozorgpour, Sanaz Karimijafarbigloo, Joseph Paul Cohen, Ehsan Adeli, and Dorit Merhof. Medical image segmentation review: The success of u-net. *arXiv preprint arXiv:2211.14830*, 2022.
- Afshin Bozorgpour, Yousef Sadegheih, Amirhossein Kazerouni, Reza Azad, and Dorit Merhof. Dermosegdiff: A boundary-aware segmentation diffusion model for skin lesion delineation. In *International Workshop on Predictive Intelligence In Medicine*, pages 146–158. Springer, 2023.
- Alexey Dosovitskiy, Lucas Beyer, Alexander Kolesnikov, Dirk Weissenborn, Xiaohua Zhai, Thomas Unterthiner, Mostafa Dehghani, Matthias Minderer, Georg Heigold, Sylvain Gelly, et al. An image is worth 16x16 words: Transformers for image recognition at scale. *arXiv preprint arXiv:2010.11929*, 2020.
- Fahad Shamsad, Salman Khan, Syed Waqas Zamir, Muhammad Haris Khan, Munawar Hayat, Fahad Shahbaz Khan, and Huazhu Fu. Transformers in medical imaging: A survey. *Medical Image Analysis*, page 102802, 2023.
- Reza Azad, Amirhossein Kazerouni, Moein Heidari, Ehsan Khodapanah Aghdam, Amirali Molaei, Yiwei Jia, Abin Jose, Rijo Roy, and Dorit Merhof. Advances in medical image analysis with vision transformers: A comprehensive review. *arXiv preprint arXiv:2301.03505*, 2023a.
- Reza Azad, Amirhossein Kazerouni, Babak Azad, Ehsan Khodapanah Aghdam, Yury Velichko, Ulas Bagci, and Dorit Merhof. Laplacian-former: Overcoming the limitations of vision transformers in local texture detection. In *International Conference on Medical Image Computing and Computer-Assisted Intervention*, pages 736–746. Springer, 2023b.
- Robert Geirhos, Patricia Rubisch, Claudio Michaelis, Matthias Bethge, Felix A Wichmann, and Wieland Brendel. Imagenet-trained cnns are biased towards texture; increasing shape bias improves accuracy and robustness. *arXiv preprint arXiv:1811.12231*, 2018.
- Jieneng Chen, Yongyi Lu, Qihang Yu, Xiangde Luo, Ehsan Adeli, Yan Wang, Le Lu, Alan L Yuille, and Yuyin Zhou. Transunet: Transformers make strong encoders for medical image segmentation. *arXiv preprint arXiv:2102.04306*, 2021.
- Moein Heidari, Amirhossein Kazerouni, Milad Soltany, Reza Azad, Ehsan Khodapanah Aghdam, Julien Cohen-Adad, and Dorit Merhof. Hiformer: Hierarchical multi-scale representations using transformers for medical image segmentation. In *Proceedings of the IEEE/CVF Winter Conference on Applications of Computer Vision*, pages 6202–6212, 2023.
- Ali Hatamizadeh, Yucheng Tang, Vishwesh Nath, Dong Yang, Andriy Myronenko, Bennett Landman, Holger R Roth, and Daguang Xu. Unetr: Transformers for 3d medical image segmentation. In *Proceedings of the IEEE/CVF winter conference on applications of computer vision*, pages 574–584, 2022.
- Yutong Xie, Jianpeng Zhang, Chunhua Shen, and Yong Xia. Cotr: Efficiently bridging cnn and transformer for 3d medical image segmentation. In *Medical Image Computing and Computer Assisted Intervention–MICCAI 2021: 24th International Conference, Strasbourg, France, September 27–October 1, 2021, Proceedings, Part III 24*, pages 171–180. Springer, 2021.
- Wenxuan Wang, Chen Chen, Meng Ding, Hong Yu, Sen Zha, and Jiangyun Li. Transbts: Multimodal brain tumor segmentation using transformer. In *Medical Image Computing and Computer Assisted Intervention–MICCAI 2021: 24th International Conference, Strasbourg, France, September 27–October 1, 2021, Proceedings, Part I 24*, pages 109–119. Springer, 2021.

- Hu Cao, Yueyue Wang, Joy Chen, Dongsheng Jiang, Xiaopeng Zhang, Qi Tian, and Manning Wang. Swin-unet: Unet-like pure transformer for medical image segmentation. In *European conference on computer vision*, pages 205–218. Springer, 2022.
- Hong-Yu Zhou, Jiansen Guo, Yinghao Zhang, Xiaoguang Han, Lequan Yu, Liansheng Wang, and Yizhou Yu. nnformer: Volumetric medical image segmentation via a 3d transformer. *IEEE Transactions on Image Processing*, 2023.
- Fan Yang, Fan Wang, Pengwei Dong, and Bo Wang. Hca-former: Hybrid convolution attention transformer for 3d medical image segmentation. *Biomedical Signal Processing and Control*, 90:105834, 2024.
- Yong Chen, Xuesong Lu, and Qinlan Xie. Collaborative networks of transformers and convolutional neural networks are powerful and versatile learners for accurate 3d medical image segmentation. *Computers in Biology and Medicine*, 164:107228, 2023.
- Abdelrahman M. Shaker, Muhammad Maaz, Hanoona Rasheed, Salman Khan, Ming-Hsuan Yang, and Fahad Shahbaz Khan. Unetr++: Delving into efficient and accurate 3d medical image segmentation. *IEEE Transactions on Medical Imaging*, 2024. doi:[10.1109/TMI.2024.3398728](https://doi.org/10.1109/TMI.2024.3398728).
- Meng-Hao Guo, Cheng-Ze Lu, Zheng-Ning Liu, Ming-Ming Cheng, and Shi-Min Hu. Visual attention network. *Computational Visual Media*, 9(4):733–752, 2023.
- Reza Azad, Leon Niggemeier, Michael Hüttemann, Amirhossein Kazerouni, Ehsan Khodapanah Aghdam, Yury Velichko, Ulas Bagci, and Dorit Merhof. Beyond self-attention: Deformable large kernel attention for medical image segmentation. In *Proceedings of the IEEE/CVF Winter Conference on Applications of Computer Vision*, pages 1287–1297, 2024.
- Md Motiur Rahman, Shiva Shokouhmand, Smriti Bhatt, and Miad Faezipour. Mist: Medical image segmentation transformer with convolutional attention mixing (cam) decoder. In *Proceedings of the IEEE/CVF Winter Conference on Applications of Computer Vision*, pages 404–413, 2024.
- Yajun Liu, Zenghui Zhang, Jiang Yue, and Weiwei Guo. Scanext: Enhancing 3d medical image segmentation with dual attention network and depth-wise convolution. *Heliyon*, 2024.
- Jing Wang, Haiyue Zhao, Wei Liang, Shuyu Wang, and Yan Zhang. Cross-convolutional transformer for automated multi-organs segmentation in a variety of medical images. *Physics in Medicine & Biology*, 68(3):035008, 2023a.
- Zhifang Hong, Mingzhi Chen, Weijie Hu, Shiyu Yan, Aiping Qu, Lingna Chen, and Junxi Chen. Dual encoder network with transformer-cnn for multi-organ segmentation. *Medical & Biological Engineering & Computing*, 61(3):661–671, 2023.
- Jiao Li, Jinyu Ye, Hongxia Deng, and Hong Shi. Cpftransformer: transformer fusion context pyramid medical image segmentation network. *Frontiers in Neuroscience*, 17:1288366, 2023.
- Bennett Landman, Zhoubing Xu, J Igelsias, Martin Styner, T Langerak, and Arno Klein. Miccai multi-atlas labeling beyond the cranial vault—workshop and challenge. In *Proc. MICCAI Multi-Atlas Labeling Beyond Cranial Vault—Workshop Challenge*, volume 5, page 12, 2015.
- Fabian Isensee, Paul F Jaeger, Simon AA Kohl, Jens Petersen, and Klaus H Maier-Hein. nnu-net: a self-configuring method for deep learning-based biomedical image segmentation. *Nature methods*, 18(2):203–211, 2021.
- Olivier Bernard, Alain Lalonde, Clement Zotti, Frederick Cervenansky, Xin Yang, Pheng-Ann Heng, Irem Cetin, Karim Lekadir, Oscar Camara, Miguel Angel Gonzalez Ballester, et al. Deep learning techniques for automatic mri cardiac multi-structures segmentation and diagnosis: is the problem solved? *IEEE transactions on medical imaging*, 37(11):2514–2525, 2018.
- Zhaohan Xiong, Qing Xia, Zhiqiang Hu, Ning Huang, Cheng Bian, Yefeng Zheng, Sulaiman Vesal, Nishant Ravikumar, Andreas Maier, Xin Yang, et al. A global benchmark of algorithms for segmenting the left atrium from late gadolinium-enhanced cardiac magnetic resonance imaging. *Medical image analysis*, 67:101832, 2021.
- Xiangde Luo, Jieneng Chen, Tao Song, and Guotai Wang. Semi-supervised medical image segmentation through dual-task consistency. In *Proceedings of the AAAI conference on artificial intelligence*, volume 35, pages 8801–8809, 2021.
- Yongchao Wang, Bin Xiao, Xiuli Bi, Weisheng Li, and Xinbo Gao. Mcf: Mutual correction framework for semi-supervised medical image segmentation. In *Proceedings of the IEEE/CVF Conference on Computer Vision and Pattern Recognition*, pages 15651–15660, 2023b.
- M Jorge Cardoso, Wenqi Li, Richard Brown, Nic Ma, Eric Kerfoot, Yiheng Wang, Benjamin Murrey, Andriy Myronenko, Can Zhao, Dong Yang, et al. Monai: An open-source framework for deep learning in healthcare. *arXiv preprint arXiv:2211.02701*, 2022.

- Holger R Roth, Le Lu, Amal Farag, Hoo-Chang Shin, Jiamin Liu, Evrim B Turkbey, and Ronald M Summers. Deeporgan: Multi-level deep convolutional networks for automated pancreas segmentation. In *Medical Image Computing and Computer-Assisted Intervention–MICCAI 2015: 18th International Conference, Munich, Germany, October 5-9, 2015, Proceedings, Part I 18*, pages 556–564. Springer, 2015.
- Spyridon Bakas, Hamed Akbari, Aristeidis Sotiras, Michel Bilello, Martin Rozycki, Justin S Kirby, John B Freymann, Keyvan Farahani, and Christos Davatzikos. Advancing the cancer genome atlas glioma mri collections with expert segmentation labels and radiomic features. *Scientific data*, 4(1):1–13, 2017.
- Bjoern H Menze, Andras Jakab, Stefan Bauer, Jayashree Kalpathy-Cramer, Keyvan Farahani, Justin Kirby, Yuliya Burren, Nicole Porz, Johannes Slotboom, Roland Wiest, et al. The multimodal brain tumor image segmentation benchmark (brats). *IEEE transactions on medical imaging*, 34(10):1993–2024, 2014.
- Reuben Dorent, Samuel Joutard, Marc Modat, Sébastien Ourselin, and Tom Vercauteren. Hetero-modal variational encoder-decoder for joint modality completion and segmentation. In *Medical Image Computing and Computer Assisted Intervention–MICCAI 2019: 22nd International Conference, Shenzhen, China, October 13–17, 2019, Proceedings, Part II 22*, pages 74–82. Springer, 2019.
- Adam Paszke, Sam Gross, Francisco Massa, Adam Lerer, James Bradbury, Gregory Chanan, Trevor Killeen, Zeming Lin, Natalia Gimelshein, Luca Antiga, et al. Pytorch: An imperative style, high-performance deep learning library. *Advances in neural information processing systems*, 32, 2019.
- William Falcon and The PyTorch Lightning team. PyTorch Lightning, March 2019. URL <https://github.com/Lightning-AI/lightning>.
- Abdel Aziz Taha and Allan Hanbury. Metrics for evaluating 3d medical image segmentation: analysis, selection, and tool. *BMC medical imaging*, 15:1–28, 2015.
- Liyao Fu, Yunzhu Chen, Wei Ji, and Feng Yang. Sstrans-net: Smart swin transformer network for medical image segmentation. *Biomedical Signal Processing and Control*, 91:106071, 2024.
- Reza Azad, Amirhossein Kazerouni, Alaa Sulaiman, Afshin Bozorgpour, Ehsan Khodapanah Aghdam, Abin Jose, and Dorit Merhof. Unlocking fine-grained details with wavelet-based high-frequency enhancement in transformers. In *International Workshop on Machine Learning in Medical Imaging*, pages 207–216. Springer, 2023c.
- Ali Hatamizadeh, Vishwesh Nath, Yucheng Tang, Dong Yang, Holger R Roth, and Daguang Xu. Swin unetr: Swin transformers for semantic segmentation of brain tumors in mri images. In *International MICCAI Brainlesion Workshop*, pages 272–284. Springer, 2021.
- Yixi Luo, Huayi Yin, and Xia Du. Moformer: Aggregating adjacent window features into local vision transformer using overlapped attention mechanism for volumetric medical segmentation. In *Proceedings of the 2022 11th International Conference on Computing and Pattern Recognition*, pages 121–127, 2022.
- Yu Ao, Weili Shi, Bai Ji, Yu Miao, Wei He, and Zhengang Jiang. Ms-tcnet: An effective transformer–cnn combined network using multi-scale feature learning for 3d medical image segmentation. *Computers in Biology and Medicine*, page 108057, 2024.
- De-Xing Huang, Xiao-Hu Zhou, Xiao-Liang Xie, Shi-Qi Liu, Zhen-Qiu Feng, Mei-Jiang Gui, Hao Li, Tian-Yu Xiang, Xiu-Ling Liu, and Zeng-Guang Hou. Mosformer: Momentum encoder-based inter-slice fusion transformer for medical image segmentation. *arXiv preprint arXiv:2401.11856*, 2024.
- Andriy Fedorov, Reinhard Beichel, Jayashree Kalpathy-Cramer, Julien Finet, Jean-Christophe Fillion-Robin, Sonia Pujol, Christian Bauer, Dominique Jennings, Fiona Fennessy, Milan Sonka, John Buatti, Stephen Aylward, James Miller, Steve Pieper, and Ron Kikinis. 3D Slicer as an Image Computing Platform for the Quantitative Imaging Network. *Magnetic Resonance Imaging*, 30(9):1323–1341, November 2012. doi:[10.1016/j.mri.2012.05.001](https://doi.org/10.1016/j.mri.2012.05.001).
- Weibin Yang, Longwei Xu, Pengwei Wang, Dehua Geng, Yusong Li, Mingyuan Xu, and Zhiqi Dong. More complex encoder is not all you need. *arXiv preprint arXiv:2309.11139*, 2023.
- Yixuan Wu, Kuanlun Liao, Jintai Chen, Jinhong Wang, Danny Z Chen, Honghao Gao, and Jian Wu. D-former: A u-shaped dilated transformer for 3d medical image segmentation. *Neural Computing and Applications*, 35(2): 1931–1944, 2023.
- Yufan He, Vishwesh Nath, Dong Yang, Yucheng Tang, Andriy Myronenko, and Daguang Xu. Swinunetr-v2: Stronger swin transformers with stagewise convolutions for 3d medical image segmentation. In *International Conference on Medical Image Computing and Computer-Assisted Intervention*, pages 416–426. Springer, 2023.
- Kisuk Lee, Jonathan Zung, Peter Li, Viren Jain, and H Sebastian Seung. Superhuman accuracy on the snemi3d connectomics challenge. *arXiv preprint arXiv:1706.00120*, 2017.

- Imad Eddine Toubal, Ye Duan, and Deshan Yang. Deep learning semantic segmentation for high-resolution medical volumes. In *2020 IEEE Applied Imagery Pattern Recognition Workshop (AIPR)*, pages 1–9. IEEE, 2020.
- Özgün Çiçek, Ahmed Abdulkadir, Soeren S Lienkamp, Thomas Brox, and Olaf Ronneberger. 3d u-net: learning dense volumetric segmentation from sparse annotation. In *Medical Image Computing and Computer-Assisted Intervention–MICCAI 2016: 19th International Conference, Athens, Greece, October 17-21, 2016, Proceedings, Part II 19*, pages 424–432. Springer, 2016.